

# Automatic Detection of Acoustic Window during Echocardiographic Imaging

Martin S Andersen, Johannes J Struijk, Samuel E Schmidt

Aalborg University, Aalborg, Denmark

## Abstract

Ultrasound remains an attractive option for cardiac imaging due to its real-time imaging capabilities and high temporal resolution. One key challenge in echocardiographic imaging is locating an optimal acoustic window for generating high-quality images. This task is confounded by the presence of anatomical structures such as ribs creating imaging shadows. This study presents an automated algorithm capable of detecting shadows. The algorithm was tested on a tissue-mimicking phantom that incorporated specular objects mimicking the acoustic shadows of ribs. The algorithm successfully detected and visualized the rib-sized objects and their accompanying shadow artifacts with a specificity of 0.73 and sensitivity of 0.76. It's implementation could enhance the accuracy and consistency of echocardiographic measurements, leading to more accurate diagnoses and improved treatment planning.

## 1. Introduction

Ultrasound is a widely used tool for cardiac diagnostics, providing clinicians with valuable anatomical and physiological information to evaluate cardiac health. Despite its widespread use, ultrasound is commonly associated with low image quality [1]. Nonetheless, ultrasound remains an attractive option due to its real-time imaging capabilities and the ability to offer high temporal resolution that can rival the electrocardiogram. However, the improvement in temporal resolution comes at the expense of image quality as the available acoustic energy for image formation is reduced due to parallel transmit-receive (TX-RX) operations [2, 3]. A further compounding of the image quality issue occurs when the transmit wave is obstructed by anatomical structures such as ribs, leading to shadows that can affect larger portions of the field of view [4, 5]. The current focus of high frame rate ultrasound has been identifying effective frameworks for improving image quality [6]. Coherent Compounding of waves uses several successive transmit emissions

pulses fired at various angles. The resulting echoes are combined to generate a single signal. This is often done simplest using in-phase and quadrature (IQ) signals [6]. Coherent Compounding has been shown to increase SNR by a factor of  $\sqrt{N}$ , where  $N$  being the number of compounded waves [7]. Coherent Compounding can use a rolling window for generating the compounded waves, to preserve frame rate. However, it should be noted, that temporal resolution will be affected, as the compounded frames are not temporally unique from each other, making it less suited for some clinical applications [2].

Harmonic imaging takes advantage of the fact that tissue behaves differently at different frequencies. When high-frequency sound waves are transmitted into the body, the tissue tends to produce sound waves at double the frequency of the transmitted waves. These higher-frequency waves are called harmonics and are more consistent and have less noise than the original transmitted waves [8].

Clutter-filters are widely used for removal of noise in echocardiographic imaging. Clutter filters can be particularly useful in imaging challenging anatomical structures, such as the heart, which is prone to ultrasound clutter due to the surrounding anatomical structures [9–11]. While some post-processing filtering do not handle shadowing and reverberation artifacts, and potentially removing clinically significant information from the ultrasound images, stationary noise filters can to some extent reduce shadows [11]. While filtering shadows has advantages, reducing the elements generating these shadows could be advantageous for guiding system operators. Here, algorithms have been created for detection of shadows or blocked transducer elements [12, 13]. Such algorithms could potentially be used for element-base amplitude correction, for optimizing the image quality [12]. The aim of this manuscript was to identify shadows, due to obscuring objects such as ribs and lungs, and thereby identifying transducer elements producing shadows during the imaging process.

## 2. Methods

The echocardiographic signal is a combination of acoustic reflections ( $s$ ) and noise  $\epsilon$ . The signal is amplified dependent on depth. The pixel is then a time-of-flight sum of the signal as defined in Equation 1.

$$\sum s + \epsilon \quad (1)$$

The idea behind the algorithm described in Section 2.1 is that if a highly specular target is introduced between the transducer and region of interest, the reflected echoes beyond the specular target will be reduced, tending towards 0. However, noise remains constant, and hence noise along the scan line  $i$  will account for a larger fraction of  $s$ . Hence a noise envelope of the  $IQ$  data could provide information regarding shadows from specular targets.

### 2.1. Algorithm

#### 1. Log compressed envelope of $IQ$ signal

$$I_{env} = 20 \log_{10}(1 + \sqrt{I^2 + Q^2}) \quad (2)$$

Where  $I$  is the in-phase and  $Q$  the quadrature, of the  $IQ$  signals.

#### 2. RMS envelope

A moving rms window size ( $S_{RMS}(\theta)$ ) was calculated using a window width  $w = 2.5\lambda$ , corresponding to 10 samples as defined in Equation 3.

$$S_{RMS}(\theta) = \sqrt{\left(\frac{1}{R} \int_R (I_{env}(\theta, r) - \mu_{I_{env}, \theta}(\theta, r))^2 dr\right)} \quad (3)$$

Where  $r$  is the pixel scan depth,  $\theta$  is the pixel angle, and  $R$  is the total scan depth of a frame, and  $\mu_{I_{env}}(\theta, r)$  being the average pixel value if the angle  $\theta$  of over the range window  $w$  centered around  $r$ .

#### 3. Identify Shadows

A beam  $\theta$  was identified as shadow, if it was a subset of a  $5^\circ$  region ( $\Phi$ ), and where all scan lines ( $\phi$ ) of a  $\Phi$  satisfy Equation 4.

$$S_{RMS}(\phi) > \mu_{S_{RMS}} \quad (4)$$

Where  $\mu_{S_{RMS}}$  denotes the average value of  $S_{RMS}$  over all scanlines  $\theta$  in the  $FOV$ .  $\theta, \phi \subset \Phi$ , and  $\Phi \subset FOV$

### 2.2. Data & Validation

Data was generated with a resolution of  $\Delta\theta = 0.5^\circ$  and  $\Delta r = 0.25\lambda$  using a tissue mimicking phantom (CIRS Model 040GSE, USA VA). Here areas of both

high and low acoustic impedance were captured with a total scan depth  $R = 120mm$  and field of view of  $FOV = 80^\circ$ , resulting in 160 scan lines per frame. To facilitate shadow generation, a 2 cm water column was placed on top of the phantom, and finger was introduced in the path of the transmit beam at various angles. Validation was done using A graphical user interface (GUI) presenting the real-time identification of shadows was utilized to superimpose overlays, highlighting the regions of shadow detection in real-time. For each frame, every scan line was annotated as either shadow or not-shadow. In a similar fashion, the algorithm denoted all scan lines in every frame as either shadow or not-shadow. Specificity, sensitivity, precision, and accuracy were then calculated from all scan lines for all frames.

## 3. Results

10 frames, with 160 scan lines each, were acquired in the CIRS tissue mimicking phantom for both high and low attenuating medium using a single TX-RX operation, resulting in a total of 20 frames or 3200 scan lines. Figure 1 shows one frame of a tissue mimicking phantom.

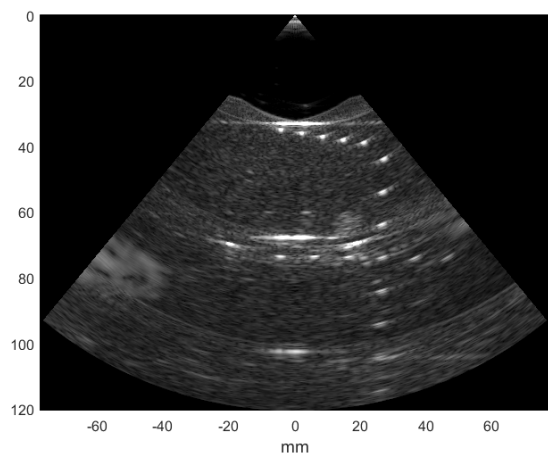


Figure 1. Frame of a tissue mimicking phantom, without any shadows. At the 25mm on the x-axis, distance markers are visible with 10mm spacing between 40mm and 110mm.

On the right side, at a depth of 40mm, distance markers can be observed, while Figure 2 shows the same view for another frame, while a bone obstructs the distance markers of the tissue mimicking phantom. Using the algorithm described in Section 2.1,  $S_{RMS}(\theta)$  was calculated for each frame, Figure 4 show

the normalized  $S_{RMS}(\theta)$  for the frame in Figure 2.

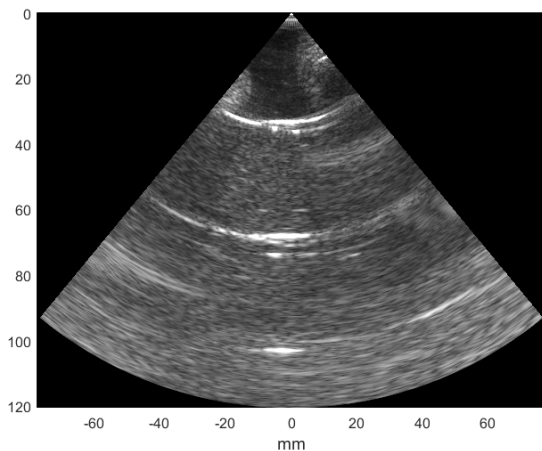


Figure 2. Frame of a tissue mimicking phantom, without any shadows. At the 25mm on the x-axis, distance markers are visible with 10mm spacing between 40mm and 110mm.

| Measurement | High att. | Low Att. | Total |
|-------------|-----------|----------|-------|
| Specificity | 0.83      | 0.66     | 0.73  |
| Sensitivity | 0.74      | 0.67     | 0.76  |
| Precision   | 0.89      | 0.67     | 0.70  |
| Accuracy    | 0.81      | 0.67     | 0.74  |
| f1Score     | 0.79      | 0.64     | 0.73  |

Table 1. Statistical results for the segmentation algorithm. The results are presented for areas with high, and low attenuation respectfully, and the combined results for all scan lines.

The resulting shadows identified by the algorithm are superimposed with the segmented shadow regions on Figure 3. The algorithm sensitivity for identifying shadows was calculated to be 0.73, precision 0.70, and accuracy 0.73, see Table 1.

#### 4. Discussion

The algorithm presented in this manuscript has been tested in a tissue-mimicking phantom, and it has shown promising results, where shadows were identified correctly in 73 % of scan lines. Further studies are required to validate its performance in a clinical setting. The algorithm's clinical potential is not limited to echocardiography, and it may have applications in other ultrasound modalities where shadows may degrade image quality, such as abdominal or lung imaging. Future directions for this research include ex-

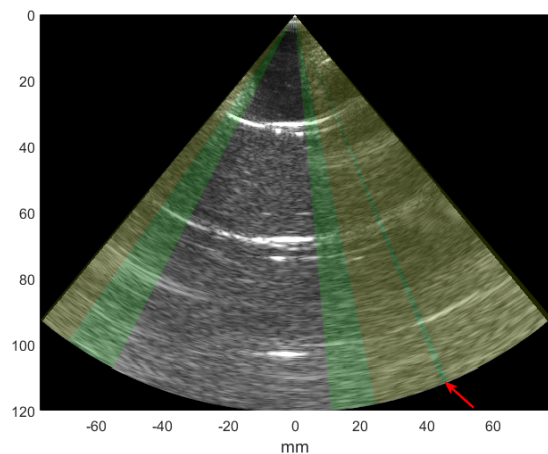


Figure 3. Frame from Figure 2 where identified and annotated shadows are superimposed on a frame. Here green represents false negative, yellow true positive, and gray true negative shadows. The red arrow denotes scanline ( $\theta = 22.5^\circ$ ) where the algorithm did not identify a shadow, see Figure 3.

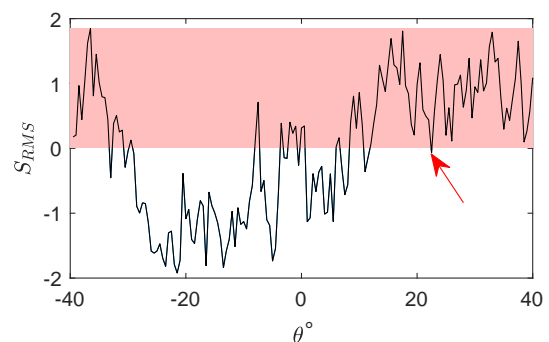


Figure 4. RMS shadow estimator ( $S_{RMS}$ ) as a function of scan lines ( $\theta$ ) denoted by the scan line angle. The red area annotates threshold for shadows. The red arrow denotes a scan line at  $\theta = 22.5^\circ$  where  $S$  is below the threshold.

ploring the algorithm's performance on a diverse patient population, optimizing the algorithm's parameters for real-time implementation. Furthermore, the algorithm's potential for reducing shadow and reverberation artifacts in dynamic element exclusion during transmit-receive operations should be explored.

#### References

- [1] Matrone G, S.Savoia A, Caliano G, Magenes G. Ultrasound plane-wave imaging with delay multiply and

- sum beamforming and coherent compounding. ISBN 9781457702204, 2016; 3223–3226.
- [2] Moore C, Castellucci J, Andersen MV, Lefevre M, Arges K, Kisslo J, Ramm OTV. Live high-frame-rate echocardiography. *IEEE Transactions on Ultrasonics Ferroelectrics and Frequency Control* 2015;62:1779–1787. ISSN 08853010.
- [3] Andersen MV, Moore C, Arges K, Søggaard P, Østergaard LR, Schmidt SE, Kisslo J, Ramm OTV. High-frame-rate deformation imaging in two dimensions using continuous speckle-feature tracking. *Ultrasound in Medicine and Biology* 2016;42:2606–2615. ISSN 1879291X.
- [4] Quien MM, Saric M. Ultrasound imaging artifacts: How to recognize them and how to avoid them, 9 2018.
- [5] Fatemi A, Torp H, Aakhus S, Rodriguez-Molares A. Increased clutter level in echocardiography due to specular reflection. volume 10139. SPIE. ISBN 9781510607231. ISSN 16057422, 3 2017; 101391D.
- [6] Poree J, Posada D, Hodzic A, Tournoux F, Cloutier G, Garcia D. High-frame-rate echocardiography using coherent compounding with doppler-based motion-compensation. *IEEE Transactions on Medical Imaging* 2016;35:1647–1657. ISSN 1558254X.
- [7] Burckhardt CB. Speckle in ultrasound b -mode scans. *IEEE Transactions on Sonics and Ultrasonics* 1978; SU-25:1–6. ISSN 00189537.
- [8] Correia M, Provost J, Chatelin S, Villemain O, Tanter M, Pernot M. Ultrafast harmonic coherent compound (uhcc) imaging for high frame rate echocardiography and shear-wave elastography. *IEEE Transactions on Ultrasonics Ferroelectrics and Frequency Control* 2016;63:420–431. ISSN 08853010.
- [9] Salles S, Lovstakken L, Aase SA, Bjastad TG, Torp H. Clutter filter wave imaging. *IEEE Transactions on Ultrasonics Ferroelectrics and Frequency Control* 9 2019;66:1444–1452. ISSN 15258955.
- [10] Hasegawa H, Nagaoka R, Omura M, Mozumi M, Saito K. Investigation of feasibility of singular value decomposition clutter filter in plane wave imaging with packet transmission sequence. *Journal of Medical Ultrasonics* 1 2021;48:13–20. ISSN 16132254.
- [11] Perperidis A. Postprocessing approaches for the improvement of cardiac ultrasound b-mode images: A review. *IEEE Transactions on Ultrasonics Ferroelectrics and Frequency Control* 3 2016;63:470–485. ISSN 08853010.
- [12] Jakovljevic M, Pinton GF, Dahl JJ, Trahey GE. Blocked elements in 1-d and 2-d arrays - part i: Detection and basic compensation on simulated and in vivo targets. *IEEE Transactions on Ultrasonics Ferroelectrics and Frequency Control* 6 2017;64:910–921. ISSN 08853010.
- [13] Huang SW, Radulescu E, Wang S, Thiele K, Prater D, Maxwell D, Rafter P, Dupuy C, Drysdale J, Erkamp R. Detection and display of acoustic window for guiding and training cardiac ultrasound users. volume 9040. SPIE. ISBN 9780819498335. ISSN 16057422, 3 2014; 904014.

Address for correspondence:

Martin Siemienski Andersen  
 Selma Lagerløfs Vej 249, 9270 Gistrup, Denmark  
 mvan@hst.aau.dk